Review

Journal of the Society of Inorganic Materials, Japan **32**, **Suppl.**, S170–S179 (2025)

High-Temperature Superplastic Deformations of Hydroxyapatite and Its Related Compounds

Kiyoshi ITATANI[1]*, Ian J. DAVIES[2], Koji MORITA[3], Tohru S. SUZUKI[3] and Yoshio SAKKA[3]

([1]Department of Materials and Life Sciences, Sophia University, 7–1 Kioi-cho, Chiyoda-ku, Tokyo 102–8554; [2]School of Civil and Mechanical Engineering, Curtin University, GPO Box U1987, Perth, WA 6845, Australia; [3]Research Center for Electronic and Optical Materials, National Institute for Materials Science, 1–2–1 Sengen, Tsukuba, Ibaraki 305–0047)

(Received Nov. 30, 2024)
(Accepted Feb. 5, 2025)

1 Introduction

Superplasticity is defined as a phenomenon in which dense and fine-grained ceramics exhibit tensile elongation-to-failure of over 100%[1),2)] or 200%[3)] at elevated temperatures. This superplastic nature may be utilized for deformation processing in the ceramics industry, *e.g.*, superplastic forming and forging[4)]. The superplastic deformation of ceramics was demonstrated in 1986 by Wakai *et al.*[5)], who found that the tensile elongation of 3 mol% yttria (Y_2O_3)-stabilized tetragonal zirconia (ZrO_2) polycrystal (3Y-TZP) attains 100% or greater at a tensile test temperature of 1450℃. Since then, many researchers have reported the superplastic deformation of oxide and non-oxide ceramics, as reviewed by Choksi[6)] (3Y-TZP and 3Y-TZP-alumina (Al_2O_3)) and Wakai *et al.*[7)] (Si_3N_4, SiC and Y-TZP).

In order to achieve superplastic deformation for practical uses, the key points to be noted are: (i) the utilization of dense ceramics with sub-micrometer- or nanometer-scaled grains[1),2)], (ii) the modification of grain-boundary properties for easy sliding (*e.g.*, the utilization of additives[1)–4)]) and (iii) the optimization of strain rate (typically, on the order of $10^{-4}\,s^{-1}$)[8)]. Owning to the control of these conditions, the tensile elongations of zirconia-related specimen achieve 550 % for 10 vol% 3Y-TZP-dispersed Al_2O_3[9)], 1,000% for 0.3 vol% Al_2O_3-dispersed TZP[10)], 1,050% for 40 vol% TZP–30 vol% magnesium aluminate spinel (MAS)–30 vol% Al_2O_3[11)] and 2,510% for 40 vol% TZP–54 vol% MAS–6 vol% Al_2O_3[12)].

Hydroxyapatite ($Ca_{10}(PO_4)_6(OH)_2$; HAp) is a chief inorganic component of human hard tissues (*i.e.*, bones and teeth) and is used in the fields of orthopedics and dentistry[13)–15)]. The superplastic deformation of HAp ceramics was demonstrated in 1990 by Wakai *et al.*[16)], who found that the tensile elongation of HAp specimen is 153%. Since then, research on the superplastic deformation of HAp ceramics is increasing in importance. The present authors have also investigated the superplastic deformations of HAp and its related calcium phosphate ceramics[17)–25)]. This review describes current research on the superplastic deformation of HAp ceramics and related calcium phosphate ceramics, together with recent progress in sintering techniques for the fabrication of high-density HAp with fine-grained ceramics.

2 Densification by pressureless sintering and superplastic deformation

The fabrication of highly-densified and fine-grained ceramics is essential to realize superplastic deformation at elevated temperature. In order to achieve high densification, any porosity needs to be excluded as much as possible from the ceramics, because the pores become the origins of the catastrophic fracture[26)]. Moreover, grain growth during sintering should be inhibited in order to enhance mechanical strength through the restriction of crack propagation along the grain boundaries[26)], due to crack pinning and deflection of the relieving stress at the crack-tip[27)]. Optimization of the starting powder properties for densification of ceramics is required to control (i) high purity, (ii) sub-micrometer- or nanometer-scale primary particles, (iii) narrow primary particle size distribution and (iv) satisfactory dispersibility of primary particles (*i.e.*, ''soft'' agglomeration)[28)].

The starting HAp nanopowder used in our research is a commercially-available high-purity product (HAP–100; Taihei Chemical Industrial, Co., Ltd., Osaka) which consists of rectangular-shaped primary particles with approximate sizes of 30 nm × 50 nm[17),18)]. High-density ceramics can be fabricated through the pressureless sintering of such HAp nanopowder (Fig. 1)[17),18)]. The relative density (per-

https://doi.org/10.11451/mukimate.25.Suppl.24

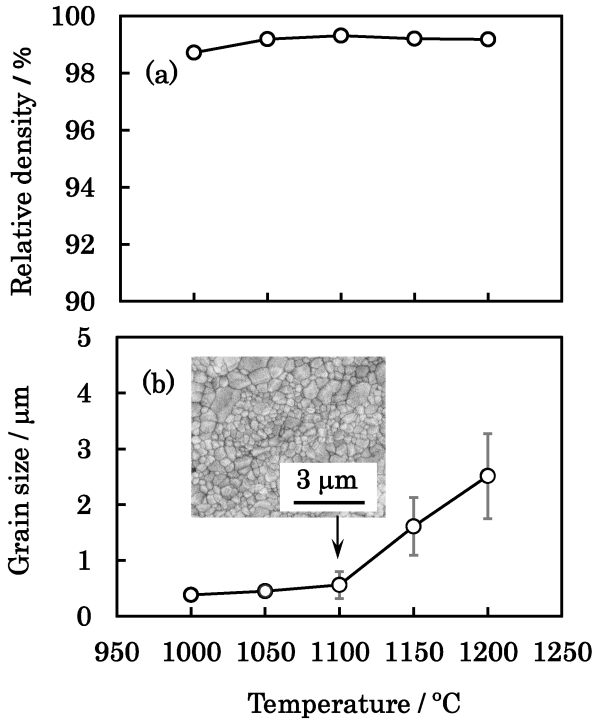

Fig. 1 Effect of firing temperature on (a) relative density and (b) grain size of sintered HAp compacts, together with a typical SEM image. Note that the HAp compact was fired at each temperature for 5 h.

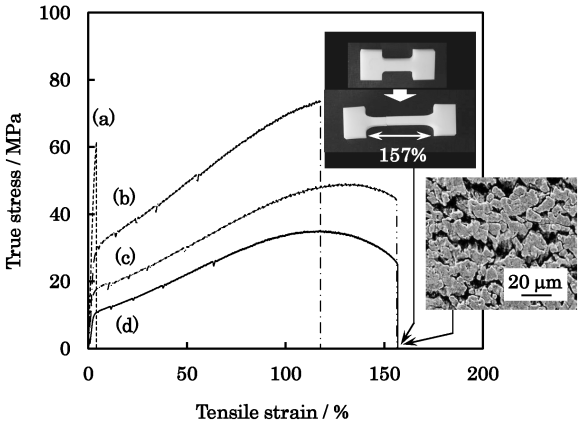

Fig. 2 Relationship between tensile strain and true stress of HAp specimens, together with a photograph showing the tensile elongation and SEM image, under the strain rate of $1.44 \times 10^{-4}\,s^{-1}$.
Tensile test temperature: (a) 940℃, (b) 1000 ℃, (c) 1050℃ and (d) 1100℃
Note that the tensile test temperatures are the same as the firing temperatures for the HAp specimens (firing time: 5 h).

centage of bulk density to theoretical density) is over 98% at 1000℃, whereas the grain size does not exceed 0.6 μm (see the image of scanning electron microscopy (SEM)). The grain growth below 1100 ℃ is inhibited not only by the delay in re-alignment of randomly oriented and nanometer-scaled crystal axes[29] but also by the ''pinning'' effect of residual pores at grain boundaries[30].

The relationship between porosity (P) and grain size (G) is empirically expressed as follows:[31]

$$GP^n = K \tag{1}$$

where n and K represent constants. Plotting the data of log G against log P indicates a straight line with the slope (n) and intercept (K). As the primary particle size decreases, the slope (n) becomes gentle, which indicates the presence of grain growth inhibition, due to the delay in the grain-boundary alignment by the randomly oriented crystallites[28].

The tensile strain-true stress curves of HAp specimens (Fig. 2)[18] illustrate that the tensile elongation at the test temperatures of 1050℃ and 1100℃ attain 156% and 157%, respectively. The microstructure following testing at 1100℃ (SEM image) indicates the formation of a significant amounts of cavities between grains.

At the test temperatures of 1050℃ and 1000℃, the cavities form in much smaller amounts on grain boundaries (Fig. 3)[18], compared to the case of 1100 ℃. The ratios of average $d_{//}$ (the grain size parallel to the tensile direction) and $d_{\perp}$ (the grain size perpendicular to the tensile direction) at 1000 and 1050 ℃ are 1.51 and 1.25, respectively, which indicate that anisotropic tensile elongation is reduced with increasing test temperature.

The strain-induced grain growth, which is regarded as dynamic grain growth, seems to preferentially occur during the initial stage of tensile elongation, accompanied by grain-boundary sliding, grain switching and grain-boundary diffusion[3),4]. The grain growth rate is generally faster than that which occurs only by annealing (static grain growth)[4),32),33].

The apparent intragranular strain (ε_g) and total strain (ε_T) are expressed as follows:[16),18),25]

$$\varepsilon_g = \frac{2}{3} \ln \frac{d_{//}}{d_{\perp}} \tag{2}$$

$$\varepsilon_T = \ln \left(\frac{L_0 + \ell}{L_0} \right) \tag{3}$$

where L_0 is the original gauge length and ℓ is the elongation at the test temperature. The contribution of grain-boundary sliding to the total strain, A, is defined as follows:

$$A = 100 \left(1 - \frac{\varepsilon_g}{\varepsilon_T} \right) \tag{4}$$

The values of A at 1000 and 1050℃ are 64.8 and 84.9%, respectively[18]. Yoshida *et al.*[34] also report the A value being 88%. These values indicate that

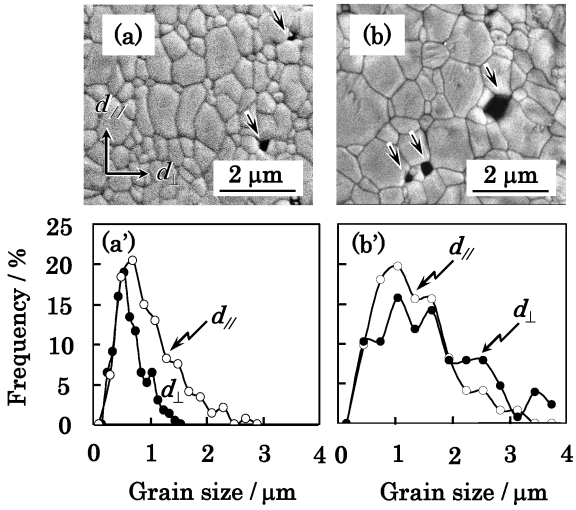

Fig. 3 SEM images of the gauge length portions of the deformed HAp specimens (above) and the grain size distributions (below) after tensile tests at 1000℃ ((a), (a′)) and 1050℃ ((b), (b′)).
Note that the arrow marks indicate the cavities and that the tensile test temperatures are the same as the firing temperatures of HAp specimens (firing time: 5 h).

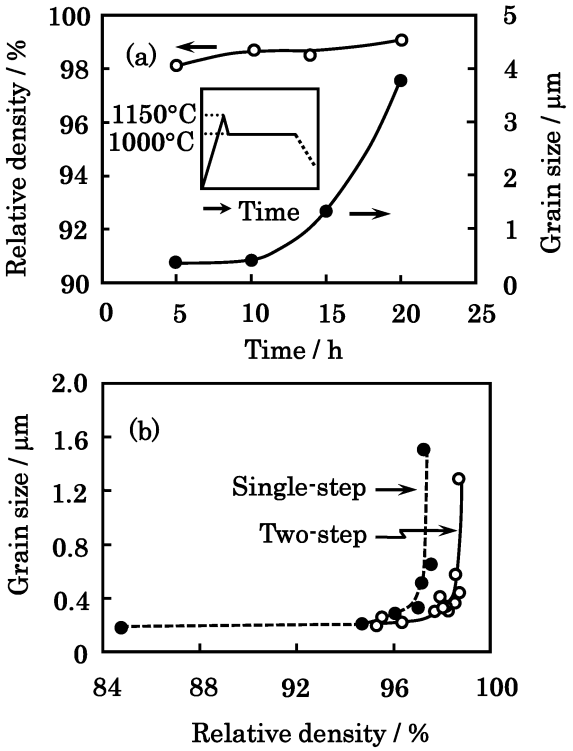

Fig. 4 (a) Changes in firing time at T_2 (=1000℃) after firing at T_1 (=1100℃) and (b) difference in relative density and grain size between single-step sintering and two-step sintering.

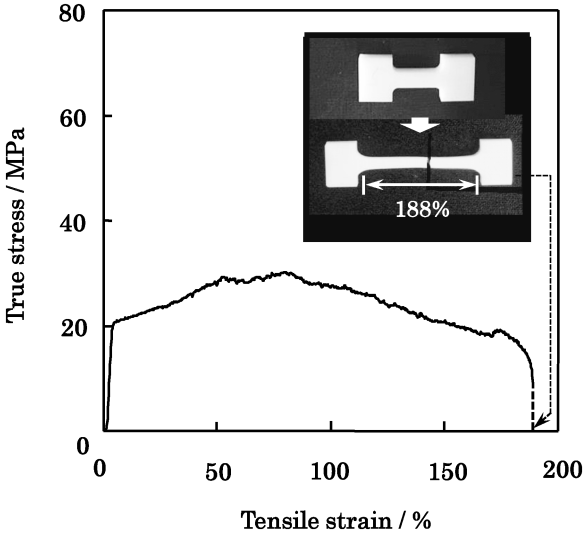

Fig. 5 Relationship between tensile strain and true stress of a HAp specimen fabricated under the conditions of T_1=1150℃, T_2=1000 and firing time=10 h, together with photographs of the HAp specimen before and after the test. Note that the test temperature and strain rate are 1000℃ and $1.44\times10^{-4}\,s^{-1}$, respectively.

grain-boundary sliding is predominant during the deformation[16),18),25),34)].

As the above information indicates, a smaller grain size is required to encourage the grain-boundary sliding. The two-step sintering process is a way to achieve the densification whilst restricting grain growth, *i.e.*, (i) heating of the powder compact to a temperature (T_1) where sintering starts in the intermediate stage, (ii) cooling to a temperature (T_2; $T_1 > T_2$) and (iii) successive holding for the desired time[19),35)]. The two-step sintering technique has been applied to oxides (*e.g.*, Y_2O_3, ZnO, Al_2O_3, Y-TZP, TiO_2, $BaTiO_3$, piezoelectric ceramics, bioceramics, *etc.*) and carbides (SiC and WC)[35)]. This technique has applied to HAp powders, *e.g.* (i) the relative density and grain size being 98.8% and 19 nm (0.19 μm), respectively, after firing at T_1=900℃ for 1 min and T_2=800℃ for 1200 min[36)], and (ii) the relative density and grain size being 99.2% and 75 nm (0.075 μm), respectively, after firing at T_1=900℃ for 5 min and T_2=850℃ for 1200 min[37)]. Plotting our grain size data against the relative density also indicates high densification whilst inhibiting grain growth. The optimization of T_1 and T_2 indicates that the relative density and grain size are 98.8% and 0.44 μm, respectively, after firing at T_1=1150℃, T_2=1000℃ for 10 h (Fig. 4(a))[19)]. Comparing to the case of single-step sintering, the two-step sintering process is effective to achieve high densification whilst inhibiting grain growth (Fig. 4(b)). Due to the grain growth inhibition, the tensile elongation of this HAp specimen increases to 188% at a test tem-

perature of 1000℃ (Fig. 5)[19].

3 Densification by pressure-assisted sintering and superplastic deformation

The advantage of sintering with an applied pressure is to significantly increase the densification rate rather than the grain growth rate, which results in high density and fine grains at low temperature[38]. Typical techniques of pressure-assisted sintering are (i) hot pressing where the pressure is uniaxially applied to the powder or powder compact in a die and (ii) hot isostatic pressing (HIP) where the pressure is isostatically applied to the powder compact by means of an inert gas[38]. As a case for utilization of HAp, Wakai *et al.*[16] showed the tensile elongation of post HIP-treated HAp specimen with a grain size of 0.64 μm to be 153%.

Pulsed current pressure sintering (PCPS) is a technique to apply a dc electric pulse under uniaxial pressure[39]. As the schematic diagram of PCPS apparatus and evolution of the Joule heating indicates (Fig. 6), the characteristics of PCPS are that the pulsed current passes through the graphite die and powder compact with an axial pressure being applied. Joule heating plays an important role in densification of the powder compact, which results in the ceramic rapidly achieving near theoretical density. This facilitates a very high heating or cooling rate (up to 1000 $K \cdot min^{-1}$), thereby generally completing densification within a few minutes. The application of PCPS to HAp powder compacts has realized the fabrication of light-transmitting HAp ceramics[23]. The transparency of HAp ceramics is enhanced by optimizing the firing temperature, time and applied pressure, *e.g.*, 1200℃ for 10 min under a pressure of 50 MPa[40] and 1000℃ for 10 min under a pressure of 80 MPa[34),41].

According to the microstructural images of high-resolution transmission electron microscopy (HR-TEM) (Fig. 7)[25], the grains with sizes of approximately 200 nm (0.2 μm) are closely packed together, in addition to pores with sizes as small as 20 nm (0.02 μm) which have little effect on light scattering (Fig. 7(a)). The lattice fringes have inter-planar spacing consistent with (100) and (210) planes of the HAp structure, whereas lattice disorder is observed at the interfaces where these atomic planes are in contact with one another (Fig. 7(b)).

Optical transparency is generally obtained through the inhibition of light scattering at the pores, due to the pore amounts and sizes being less than 1% and nanometer scale (<100 nm), respectively[42]. In addition, light scattering at grain boundaries, due to the discontinuity of refractive index (*i.e.*, difference in crystallographic orientations) and presence of point defects, are minimized with decreasing grain size[42),43]. According to the high-resolution TEM observation of pressurelessly-sintered HAp ceramics conducted by Kleebe *et al.*[44], no indication of amorphous phase is observed at multigrain junctions. In contrast to pressureless sintering, PCPS is conducted by Joule heating which is triggered by a high-density current due to the inter-particle contacts and

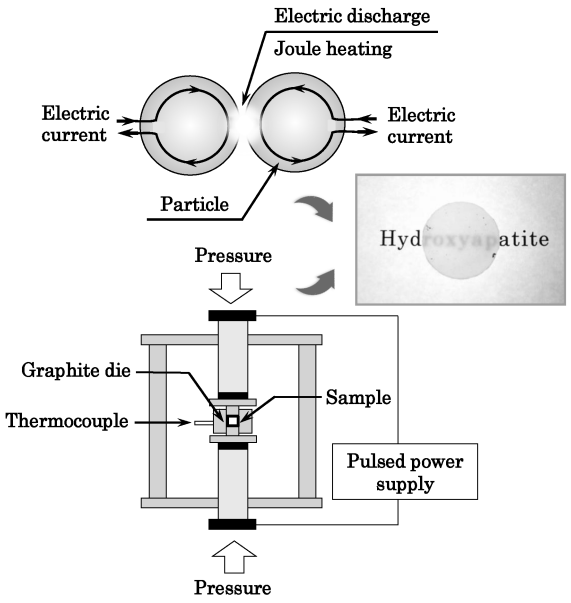

Fig. 6 Schematic diagram of PCPS apparatus and path routes of pulse current, together with a photograph illustrating the translucency of HAp ceramics fabricated by PCPS.

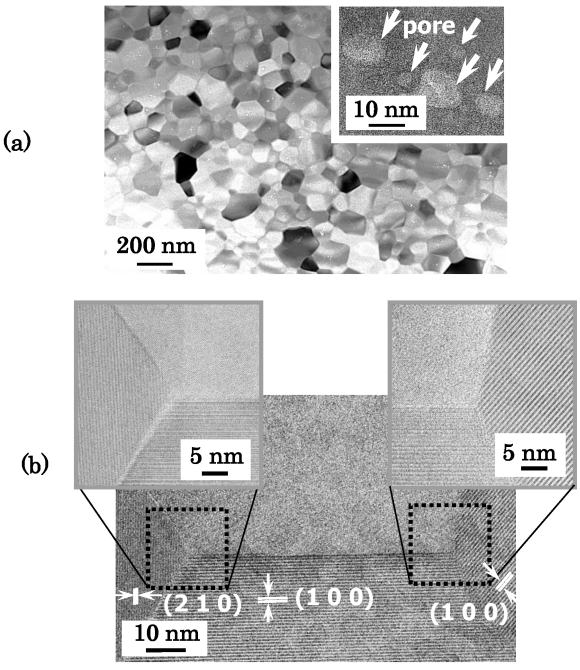

Fig. 7 HR-TEM images of a HAp specimen fabricated by PCPS at 1000℃ for 10 min.
(a) Overall view (b) Lattice images

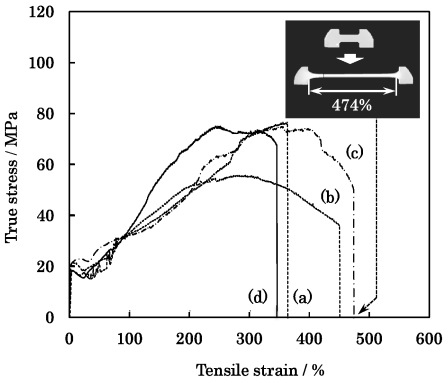

Fig. 8 Relationship between tensile strain and true stress of HAp specimens tested at 1000℃ under the strain rates of (a) 1.5×10^{-4}, (b) 3.0×10^{-4}, (c) 5.9×10^{-4} and (d) 12×10^{-4} s^{-1}, together with a typical photograph of the original and elongated specimens.

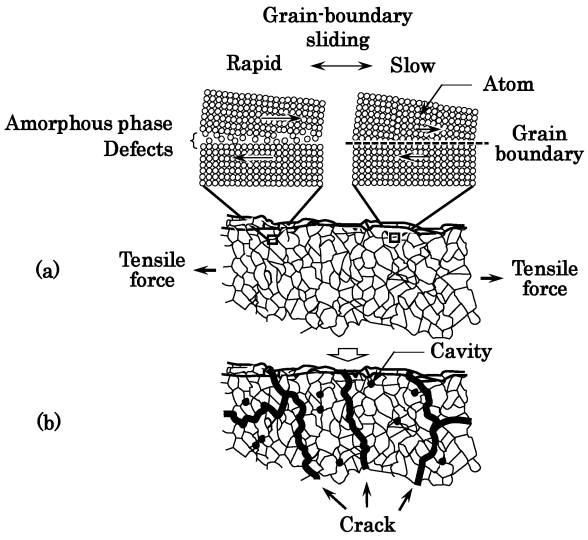

Fig. 9 Schematic diagram of the microstructure changes for a HAp specimen, due to the application of tensile force.
(a) Original microstructure of HAp specimen before the tensile elongation, together with the alignment of atoms at and near the grain boundaries
(b) Fracturing of HAp specimen following tensile elongation

concentrated in the grain-boundary region, thereby producing high local temperatures at the contacts of particles[39]. Such local high temperatures have the possibility to alter the properties of grain boundaries, *e.g.*, owing to the formation of amorphous phase and defects.

The relationship between tensile strain and true stress of HAp specimens (Fig. 8)[22], as a function of strain rate, indicates that the tensile elongation of HAp specimens exhibits a maximum (474%) at a strain rate of 5.9×10^{-4} s^{-1} (see photograph). The mean grain size increases from 0.2 to 4.1 μm with increasing tensile elongation[22], due to the combined effects of grain-boundary sliding and grain switching accommodated by diffusion[3]. The fracturing mechanism may be attributed to inoperative grain-boundary sliding, based on cavity formation and grain growth. Similar results on the tensile elongation have been obtained by Yoshida *et al.*[34], who showed the tensile elongation to be 486% at a test temperature of 1000℃ under a strain rate of 1.0×10^{-4} s^{-1}.

As the illustration of tensile elongation at high temperature indicates (Fig. 9), the grain-boundary sliding occurs when amorphous phases and defects are present on the grain boundaries. The larger amount of amorphous phase encourages grain-boundary sliding, whereas a smaller amount of amorphous phase facilitates grain growth due to the migration of atoms (Fig. 9(a)). When the strain rate exceeds the grain-boundary sliding rate, then catastrophic fracturing occurs (Fig. 9(b)).

The chief deformation mechanism of HAp specimens seems to be due to dislocation related grain-boundary sliding, which assumes the activated motion of dislocations as a sink and source of vacancies on grain boundaries[45]. When grain-boundary sliding is facilitated by intragranular dislocation movement, lattice diffusion is the rate controlling process[45]. Taking into the consideration of hexagonal and monoclinic HAps which exhibit an anisotropic crystallographic structure[46], the grains are likely to grow faster in the stress direction when compared to other directions[45].

4 Superplastic deformation of HAp specimen with boron oxide addition

As mentioned above, the presence of amorphous phases and defects on the grain boundaries are crucial to assist the superplastic deformation of HAp specimens. One method to create amorphous phases and/or defects is through the utilization of additives. Such additives react with matrix to form secondary phases which are segregated on and near the grain boundaries.

Amongst additives utilized for the encouragement of superplastic deformation of HAp specimens, boron oxide (B_2O_3) is a promising additive[22),23]. The phosphate and OH groups of HAp are partially substituted by borate groups, as expressed by the chemical formula of $Ca_{10}\{(PO_4)_{6-x}(BO_3)_x\}\{(BO_3)_y(BO_2)_z(OH)_{2-3y-z}\}$[47]. Such a solid solution also contributes not only to decreasing the thermal decomposition of HAp but also enhancing the bending strength and fracture toughness[48]. According to the tensile strain-true stress curves of HAp specimens with 3.0 mol% addition (Fig. 10)[22),23], the tensile elongation of

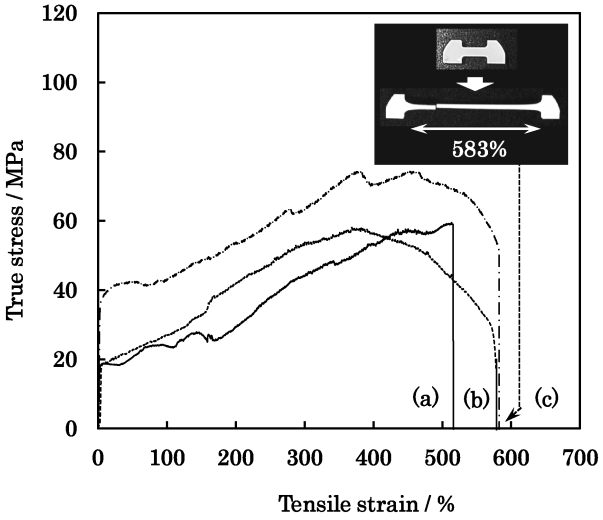

Fig. 10 Changes in true strain for HAp specimen with 3.0 mol% B_2O_3 addition as the tensile stress increases at the tensile test temperature of 1000℃ under the strain rates of (a) 1.5×10^{-4}, (b) 5.9×10^{-4} and (c) 24×10^{-4} s^{-1}, together with a typical photograph of the original and elongated specimens.

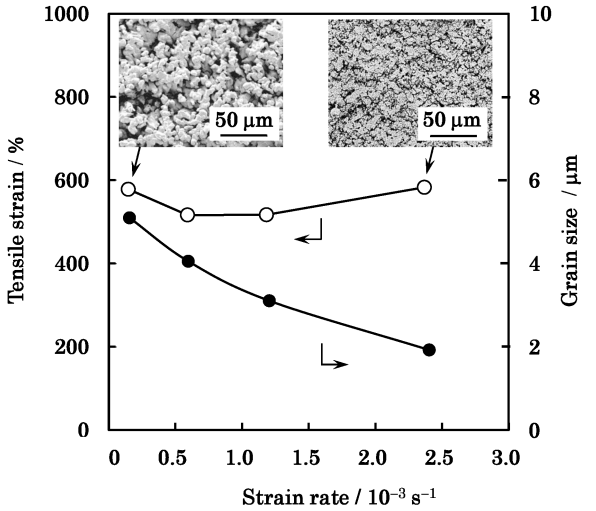

Fig. 11 Changes in tensile strain and grain size of HAp specimens with 3.0 mol% B_2O_3 addition as the tensile rate increases at the tensile test temperature of 1000℃, together with typical SEM images of the elongated specimens.

HAp specimen with 3.0 mol% addition shows a maximum (583%) at the strain rate of 24×10^{-4} s^{-1}.

The relationship between strain rate and tensile strain (Fig. 11) indicates that no marked difference in tensile elongation, regardless of the decrease in grain size, is found with increasing strain rate from 1.5 to 24×10^{-4} s^{-1}. According to the SEM images of the elongated HAp specimens, the cavities

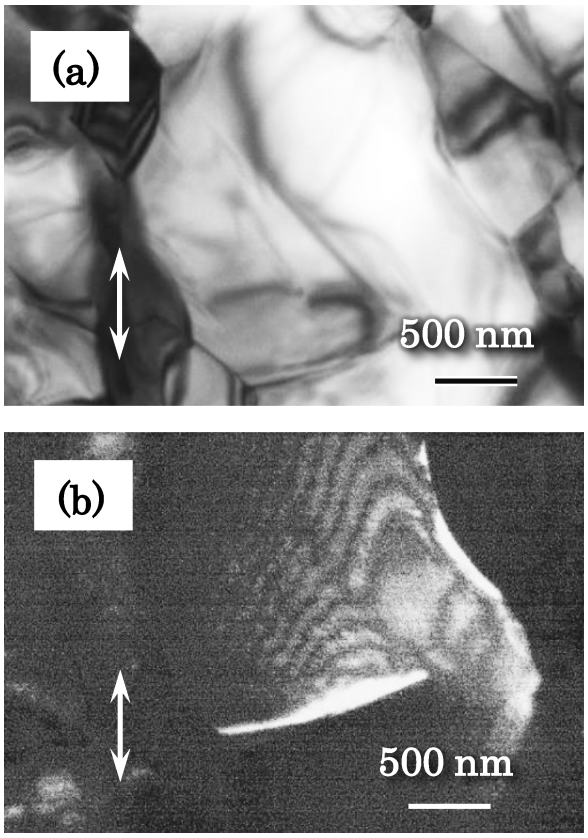

Fig. 12 (a) Bright field HR-TEM image and (b) dark field HR-TEM image of a HAp specimen with 3.0 mol% B_2O_3 addition after fracturing at the tensile temperature of 1000℃ under a strain rate of 12×10^{-4} s^{-1}. Note that the arrow marks indicate the direction of applied pressure.

become homogeneously present with increasing strain rate. Of particular note is to mention that the elongation-to-fracture time of the HAp specimen is reduced approximately from 12 h to only 45 min with increasing strain rate, regardless of the significant tensile elongations close to 600%.

Checking the HR-TEM bright field and dark field images of HAp specimen with 3.0 mol% B_2O_3 addition (Fig. 12), the deformed grains are observed in parallel to the elongation (bright field image; Fig. 12 (a)). On the other hand, the dark-field TEM image indicates that the striped lines show the presence of concentrated strains within the crystal lattice and/or the presence of dislocations (Fig. 12(b)), which are introduced during tensile elongation[49)–51)].

Dynamic grain growth during tensile elongation is related to the strain (ε) as follows:[4)]

$$\ln\frac{d}{d_0}=B\varepsilon \qquad (5)$$

where d_0 and d are the grain sizes before and after deformation, respectively, and B is a proportionality

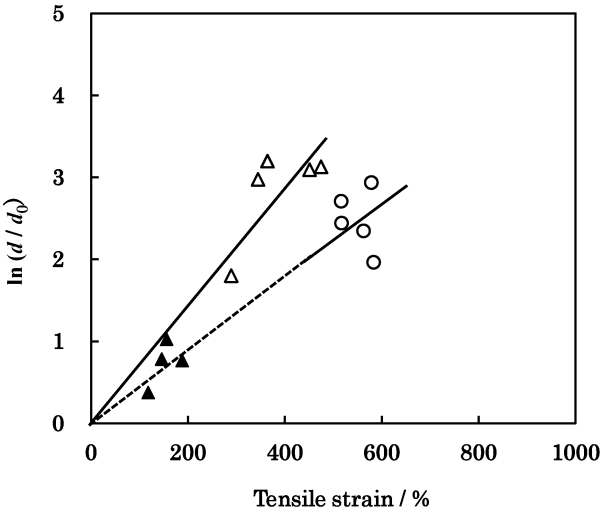

Fig. 13 Relationship between grain size and tensile strain of HAp specimens after tensile testing.
▲: Pressureless sintering of HAp specimen
△: PCPS of HAp specimen
○: PCPS of HAp specimen with 3.0 mol% B_2O_3 addition

constant that couples the strain rate through grain-boundary migration. The linear correlations between ln (d/d_0) and ε gives B values for HAp specimens with and without B_2O_3 addition of 7.05×10^{-3} and 4.48×10^{-3}, respectively (Fig. 13). The gentle slope obtained through the addition of B_2O_3 indicates the dominant deformation of grain-boundary sliding to have occurred during tensile elongation. Although static grain growth also occurs during the tensile deformation, the straight line which passes through the origin suggests that the main contribution to grain growth is based on the dynamic grain growth[4),32),52)].

5 Effect of molecular structure on the superplastic deformation

The chemical formula of calcium apatite is expressed as $Ca_{10}(PO_4)_6X_2$ (X=OH, F, Cl). Through replacing the hydroxyl group with fluorine ions, *i.e.*, fluorapatite ($Ca_{10}(PO_4)_6F_2$: FAp), the effect of terminal group on the tensile elongation can be evaluated. High density FAp specimens with sub-micrometer-scale grains[20),53)], *e.g.*, relative density of 98.8% and mean grain size of 0.79 μm, have been fabricated using the PCPS technique[20)]. Tensile elongation at the test temperature of 1100℃ was 70.6%[20)]. On the basis of these results, the higher tensile elongation of HAp specimens, compared to that of FAp specimens, is related to the presence of defects which are essential for assisting grain-boundary sliding, because the vacancies in OH sites of HAp are created at high temperature through dehydroxylation to form oxyhydroxyapatite ($Ca_{10}(PO_4)_6(OH)_{2-2x}O_x\square_x$: $\square$= vacancy, $x<1$[54),55)]).

$$Ca_{10}(O_4)_6(OH)_2 \rightarrow Ca_{10}(PO_4)_6(OH)_{2-2x}O_x\square_x + xH_2O \quad (6)$$

The dehydroxylation of OH sites in HAp is also confirmed by the contraction of lattice constants and unit cell volumes through X-ray diffraction[56)]. In addition to these apatites, Adachi *et al.*[57)] report the superplastic deformation of carbonate apatite. Thus, the control of terminal groups in the X-site of the apatite structure seems to be important for superplastic deformation. Relating to the framework of the CaO-P_2O_5 structure, the tensile elongation of β-tricalcium phosphate (β-$Ca_3(PO_4)_2$) specimen with mean grain size of 0.78 μm is 145% at the test temperature of 1000℃[21)]. As the data so far reported indicates, the apatites and their related calcium phosphates ceramics have the potential to exhibit superplastic deformation.

6 Concluding remarks

The present review describes the superplastic deformation of HAp and its related compounds at high temperature. The notable superplastic deformation of HAp specimens has been successfully realized by the utilization of high-density HAp specimens with sub-micrometer-scale grains fabricated through pressureless sintering (single-step and two-step sintering) and pressure-assisted sintering (HIP and PCPS). The continuous advancement of sintering techniques to fabricate high-density HAp with fine-grained ceramics is expected to further enhance the superplastic deformation, getting closer to their utilization in practical applications.

References

1) Y. Maehara, T. G. Langdon, *J. Mater. Sci.*, **25**, 2275–2286 (1990).
2) T. G. Langdon, *J. Mater. Sci.*, **44**, 5998–6010 (2009).
3) K. Hiraga, B.-N. Kim, K. Morita, T. S. Suzuki, Y. Sakka, *J. Ceram. Soc. Japan*, **113**, 191–197 (2005).
4) I-W. Chen, L. A, Xue, *J. Am. Ceram. Soc.*, **73**, 2585–2609 (1990).
5) F. Wakai, S. Sakaguchi, Y. Matsuno, *Adv. Ceram. Mater.*, **1**, 259–263 (1986).
6) A. H. Chokshi, *Mater. Sci. Eng.*, **A166**, 119–133 (1993).
7) F. Wakai, N. Kondo, Y. Shinoda, *Curr. Opin. Solid State Mater. Sci.*, **4**, 461–465 (1999).
8) M. A. Nazzal, M. K. Khraisheh, F. K. Abu-Farha, *J. Mater. Proc. Technol.*, **191**, 189–192 (2007).
9) Y. Sakka, K. Hiraga, *Nihon Kagaku Kaishi*, **1999**, 497–508 (1999) [in Japanese].
10) Y. Sakka, T. S. Suzuki, K. Morita, K. Nakano, K. Hiraga, *Scripta Mater.*, **44**, 2075–2078

(2001).
11) B.-N. Kim, K. Hiraga, K. Morita, Y. Sakka, *Nature*, **413**, 288–291 (2001).
12) B.-N. Kim, K. Hiraga, K. Morita, Y. Sakka, T. Yamada, *Scripta Mater.*, **47**, 775–779 (2002).
13) K. Pajor, L. Pajchel, J. Kolmas, *Materials*, **12**, 2683 (2019).
14) G. Ulian, D. Moro, G. Valdrè, *Biomolecules*, **11**, 728 (2021).
15) R. O. Kareem, N. Bulut, O. Kaygili, *J. Chem. Rev.*, **6**, 1–26 (2024).
16) F. Wakai, Y. Kodama, S. Sakaguchi, T. Nonami, *J. Am. Ceram. Soc.*, **73**, 457–460 (1990).
17) K. Tago, K. Itatani, S. Koda, *Phos. Res. Bull.*, **19**, 250–255 (2005).
18) K. Tago, K. Itatani, T. S. Suzuki, Y. Sakka, S. Koda, *J. Ceram. Soc. Japan*, **113**, 669–673 (2005).
19) K. Itatani, A. Kobayashi, D. Watanabe, I. J. Davies, S. Koda, *J. Soc. Inorg. Mater. Japan*, **16**, 8–14 (2009).
20) D. Watanabe, Y. Sakka, I. J. Davies, S. Koda, K. Itatani, *Phos. Res. Bull.*, **23**, 45–51 (2009).
21) D. Watanabe, K. Nishio, Y. Sakka, M. Ohgaki, I. J. Davies, T. Umeda, S. Koda, K. Itatani, *J. Mater. Sci.*, **46**, 1956–1962 (2011).
22) K. Itatani, K. Tsuchiya, Y. Sakka, I. J. Davies, S. Koda, *Mater. Sci. Eng.*, **18**, 022020 (2011).
23) K. Itatani, K. Tsuchiya, Y. Sakka, I. J. Davies, S. Koda, *J. Eur. Ceram. Soc.*, **31**, 2641–2648 (2011).
24) Y. Asano, Y. Sakka, I. J. Davies, S. Koda, K. Itatani, *Phos. Res. Bull.*, **27**, 11–17 (2012).
25) R. Yamazaki, K. Morita, Y. Sakka, K. Itatani, *Adv. Mater. Lett.*, **7**, 130–135 (2016).
26) R. W. Rice, *J. Mater. Sci.*, **19**, 895–914 (1984).
27) Z. Gong, W. Zhao, K. Guan, P. Rao, Q. Zeng, J. Liu, Z. Feng, *J. Am. Ceram. Soc.*, **103**, 5900–5913 (2020).
28) K. Itatani, R. Yamazaki, H. Mori, I. J. Davies, S. Kajiwara, H. Kuroe, H. Minamisawa, Y. Kojima, *J. Soc. Inorg. Mater. Japan*, **31**, 17–24 (2024).
29) J. M. Sestito, F. Abdeljawad, T. A. L. Harris, Y. Wang, A. Roach, *Comput. Mater. Sci.*, **165**, 180–189 (2019).
30) V. Rehn, J. Hötzer, W. Rheinheimer, M. Seiz, C. Serr, B. Nestler, *Acta Mater.*, **174**, 439–449 (2019).
31) G. C. Kuczynski, in Sintering and Related phenomena (Mater. Sci. Res. Vol. 6) edited by G. C. Kuczynski, Plenum Press, New York-London (1973) pp. 217–224.
32) T.-G. Nieh, J. Wadsworth, *J. Am. Ceram. Sac.*, **72**, 1469–72 (1989).
33) F. Wakai, *J. Ceram. Soc. Japan*, **112**, 472–476 (2004).
34) H. Yoshida, B.-N. Kim, H.-W. Son, Y.-H. Han, S. Kim, *Script. Mater.*, **69**, 155–158 (2013).
35) N. J. Lóh, L. Simão, C. A. Faller, A. D. Noni Jr, O. R. K. Montedo, *Ceram. Int.*, **42**, 12556–12572 (2016).
36) M. Mazaheri, M. Haghighatzadeh, A. M. Zahedi, S. K. Sadrnezhaad, *J. Alloys Comp.*, **471**, 180–184 (2009).
37) M. J. Lukić, S. D. Škapin, S. Marković, D. Uskoković, *J. Am. Ceram. Soc.*, **95**, 3394–3402 (2012).
38) M. N. Rahaman, Ceramic Processing and Sintering, Marcel Dekker, New York, Basel, (1995) pp. 735–752.
39) X. Y. Li, Z. H. Zhang, X. W. Cheng, G. J. Huo, S. Z. Zhang, Q. Song, *Powder Metall. Met. Ceram.*, **60**, 410–438 (2021).
40) Y. Watanabe, T. Ikoma, A. Monkawa, Y. Suetsugu, H. Yamada, J. Tanaka, Y. Moriyoshi, *J. Am. Ceram. Soc.*, **88**, 243–245 (2005).
41) B.-N. Kim, E. Prajatelistia, Y.-H. Han, H.-W. Son, Y. Sakka, S. Kim, *Script. Mater.*, **69**, 366–369 (2013).
42) Y. Kodera, C. L. Hardin, J. E. Garay, *Scrip. Mater.*, **69**, 149–154 (2013).
43) A. A. Gandhi, R. D. Gunning, K. M. Ryan, S. A. M. Tofail, *J. Am. Ceram. Soc.*, **93**, 3773–3777 (2010).
44) H.-J. Kleebe, E. F. Bres, D. Bernache-Assolant, G. Ziegler, *J. Am. Ceram. Soc.*, **80**, 37–44 (1997).
45) J. Yun, B. N. Kim, Y. H. Han, H. W. Son, S. Kim, H. Yoshida, *Adv. Appl. Ceram.*, **114**, 175–177 (2015).
46) D. Haverty, S. A. M. Tofail, K. T. Stanton, J. B. McMonagle, *Phys. Rev. B*, **71**, 094103 (2005).
47) R. Ternane, M. Th. Cohen-Adad, G. Panczer, C. Goutaudier, N. Kbir-Ariguib, M. Trabelsi-Ayedi, P. Florian, D. Massiot, *J. Alloys Compd.*, **333**, 62–71 (2002).
48) Y. Chun, G. Ying-kui, Z. Mi-lin, *Trans. Noferrous Met. Soc. China*, **20**, 254–258 (2010).
49) D. Singh, M. de la Cinta Lorenzo-Martin, J. L. Routbort, F. Gutiérrez-Mora, E. D. Case, *Int. J. Appl. Ceram. Technol.*, **2**, 247–255 (2005).
50) H. Saka, D. Goto, W.-J. Moon, *J. Mater. Sci.*, **43**, 3234–3239 (2008).
51) V. M. Ievlev, S. M. Barinov, V. S. Komlev,

A. Yu. Fedotov, A. V. Kostyuchenko, A. R. Kilmametov, J. V. Rau, S. V. Dobatkin, *Ceram. Int.*, **41**, 10526–10530 (2015).
52) L. A. Xue, X. Wu, I-W. Chen, *J. Am. Ceram. Soc.*, **74**, 842–45 (1991).
53) H. Furuse, D. Kato, K. Morita, T. S. Suzuki, B. -N. Kim, *Materials*, **15**, 8157 (2022).
54) T. Kijima, M. Tsutsumi, *J. Am. Ceram. Soc.*, **62**, 455–460 (1979).
55) N. V. Bulina, S. V. Makarova, S. G. Baev, A. A. Matvienko, K. B. Gerasimov, O. A. Logutenko, V. S. Bystrov, *Minerals*, **11**, 1310 (2021).
56) S. M. Barinov, L. I. Shvorneva, D. Ferro, I. V. Fadeeva, S. V. Tumanov, *Sci. Tech. Adv. Mater.*, **5**, 537–541 (2004).
57) M. Adachi, N. Wakamatsu, Y. Doi, *Dent. Mater. J.*, **27**, 93–98 (2008).

水酸アパタイトおよび関連化合物の高温超塑性変形

板谷　清司[1*]・Ian J. DAVIES[2]・森田　孝治[3]・鈴木　達[3]・目　義雄[3]
([1]上智大学理工学部物質生命理工学科，[2]School of Civil and Mechanical Engineering, Curtin University, [3]物質・材料研究機構電子・光機能材料研究センター)

本解説ではサブミクロンサイズの結晶粒から成る水酸アパタイト($Ca_{10}(PO_4)_6(OH)_2$:HAp) および関連化合物の高温超塑性について述べる．これらの化合物の高密度セラミックスは無加圧焼結法(一段階および二段階焼結)や加圧焼結法(熱間等方加圧およびパルス通電加圧)によって作製することができる．高密度 HAp セラミックスの高温引張り試験を最適な加熱温度および歪み速度の条件下で行うと，粒界すべりや結晶粒のスイッチングが促されることによって引張り歪みは 600%近くまで増加する．